End of Master Degree Project

Master of Science in Mechanical Engineering ETH

Micro Computed Tomography Based Finite Element Models of Calcium Phosphate Scaffolds for Bone Tissue Engineering

Author: Timo Jung

Director/s: Dr. Clara Sandino

Call: October 2016

Escola Tècnica Superior

d'Enginyeria Industrial de Barcelona

Abstract

Timo Jung , Micro Computed Tomography Based Finite Element Models of Calcium Phosphate Scaffolds for Bone Tissue Engineering

Bone is a living tissue that is able to regenerate by itself. However, when severe bone defects occur, the natural regeneration may be impaired. In these cases, bone graft substitutes can be used to induce the natural healing process. As a scaffold for tissue engineering, synthetic bone graft substitutes have to meet specific requirements. Among others, the material must be biocompatible, biodegradable and have a porous structure that allows vascularisation, cell migration and formation of new bone. Additionally, the mechanical properties of the scaffold have to resemble the ones of the native tissue.

Robocasting, a method to fabricate complex and customized structures, has the potential to produce scaffolds that have both appropriate mechanical properties but also include the required porosity. Analysing candidates for structures becomes a new problem, however. This study therefore introduces a simulation process that allows to determine the apparent stiffness and strength of a scaffold based on its micro-architecture. The simulation can be based on micro computed tomography images of the scaffold or on the initial design file. It uses the finite element modeling technology to calculate not only the apparent mechanical properties but also local strains. Additionally, it includes different yield criteria for the modelling of the failure of the scaffold.

Moreover, three different patterns that were used in a previous study to print calcium phosphate scaffolds were analysed using the developed simulation process and the results were compared to the results of mechanical testing. Even though the simulation process overestimates the mechanical properties of the scaffold, it manages to predict the general behaviour of the individual scaffolds well, especially when it is based on the design files.

Acknowledgements

First I thank Prof. Dr. Maria Pau Ginebra for allowing me to do my Master's Thesis at the Biomaterials, Biomechanics and Tissue Engineering Research Group and giving me encouraging and supporting words.

I am grateful for the support I got from my supervisor Dr. Clara Sandino. She always took the time to help me out with some advice or new ideas and never avoided any effort to assist me in the tasks, no matter how busy she herself was. I am very happy that I got such a patient and competent coach.

I also want to express my gratitude towards the Mobility Offices of both the UPC and the ETH. They were very helpful and supportive even when bothered with tight deadlines.

Special thanks go to Anna Diez, Giuseppe Scionti and Meritxell Molmeneu for their help in the lab and to Edgar Montufar, Yassine Maazouz and Yago Raimond for providing required data.

Moreover I am thankful to all the people of the research group. It was a great joy to work with them all and I will not forget the hours spent with them.

Last but not least, I thank my family and friends for always being there for me and helping me out of whatever problem and sorrow I could possibly have.

Contents

List of Figures

Nomenclature

In the following table, a notation is introduced that will be applied throughout this report.

FE model	Abbreviation for finite element model. Always stands for the mesh of the scaffold together with the material properties and the boundary conditions.
Simulation process	Stands for a series of FE models, resulting in the calculation of a whole compression test.
Failure	Always concerns single or several elements of the finite element mesh, where the stress from the FE model calculation exceeds the ultimate strength of the material.
Fracture	Represents the separation of the scaffold into several pieces in the actual compression test.
3D-printing	Abbreviation for three dimensional printing. Rapid prototyping technology. In this report interchangebly used with robocasting. A technology to print three-dimensional structures by depositing layers of filaments through a nozzle system.
μCT	Abbreviation for micro computed tomography. Imaging system that uses x-rays to obtain images of cross sections of an object with a resolution in the micrometer range. The sequence of cross sections can be used to create a virtual model of the original object.
Apparent properties	Properties of a scaffold taking into account both the material properties and the structure of the scaffold.

Chapter 1

Introduction

1.1 Bone Tissue Engineering

Native bone is known to be constantly degrading and rebuilding parts of its framework. Thanks to this permanent remodeling process, bone is able to not only adapt to a change in its loading condition but also fix defects and fractures by itself [1]. However, major defects, e.g. resulting from trauma or tumors, can not be fixed at all or only insufficiently [2].

Bone tissue engineering steps in at this point. The goal of bone tissue engineering is to repair the defect in the native tissue by forming a substitute in vitro that can then be implanted. To be able to perform this complicated task, various methods from different fields of science have to be combined. An important role for example is played by biological, physiomechanical and biochemical factors, illustrated in Figure 1.1 [3]. Within these factors, the scaffold that is used as a basis for the substitute is crucial. Since it has to allow cells to seed, proliferate and differentiate into new tissue, it has to consist of a biocompatible and biodegradable material. But also its structure is subjected to several requirements [4]. For instance in the case of porous scaffolds, the apparent mechanical properties of the structure have to resemble the ones of native bone. Such a scaffold would allow an early load bearing of the defect bone so that the functionality of the tissue is restored fast. However, the porosity is at the interface of two rivalling mechanisms. On the one hand a high porosity decreases the stiffness and strength of the scaffold. On the other hand, an interconnected network of large pores has to exist so that cells can migrate throughout the scaffold and be provided with nutrients and growth factors through vascularisation. A high porosity would be beneficial for these processes. Therefore, for the success of a porous scaffold, a structure that results in apparent properties similar to native bone but still allows cell migration and vascularistation, has to be found[5].

[1] Image source: [3]

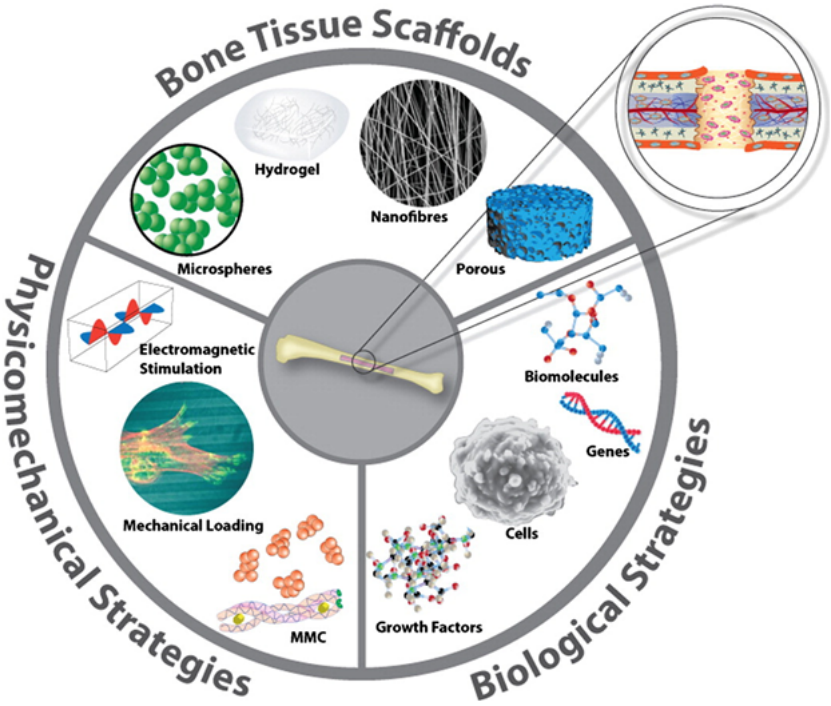

Figure 1.1: Influencing Factors of Bone Tissue Engineering - This figure shows bone tissue engineering at the interface of many different subjects.[1]

1.2 Three Dimensional Printing

There are a lot of different fabrication methods to produce a porous scaffold. Conventional methods include among others solvent casting, gas foaming or freeze drying. Those methods however, often have the disadvantage, that parameters like the pore sizes, pore distributions and structure can not be controlled precisely [6]. One approach to overcome these issues is rapid prototyping. It includes several different technologies, including the three-dimensional (3D) printing, that has become very popular over the last few years [7]. It is based on the use of a design file that includes the exact structure of the scaffold. By depositing a filament through a nozzle in a controlled manner, the desired structure is built layer by layer, as shown in Figure 1.2. This approach allows the fabrication of customized and complex shapes, thereby giving direct control over the porosity of the scaffold [8] [9].

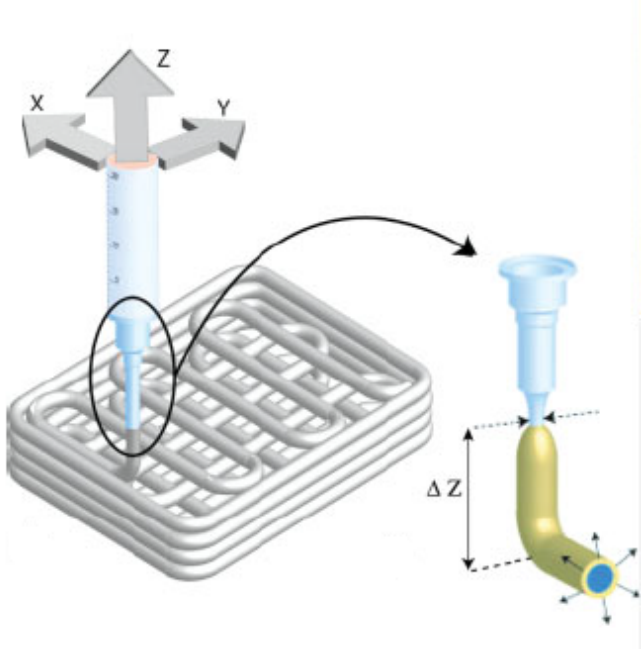

Figure 1.2: Robocasting Process - This figure shows the process of creating a scaffold by 3D-printing. Note that during the setting process, the filament diameter can change due to swelling.[2]

1.3 Calcium Phosphate Scaffolds

One promising material serving as a scaffold in bone tissue engineering is calcium phosphate (CaP). The main advantage of the CaP is its similarity to the mineral phase of

[2]Image source: [9]

bone [10]. Other advantages are the biodegradability with a rate that closely matches the formation rate of new bone [11], the osteoconductivity of the material [12] and the intrinsic porosity in the micro- and nanoscale [13]. Another feature of special interest is that the CaP can be produced in the form of an injectable paste, called CaP cement. Not only could they therefore be injected into the human body where they harden after their application, but they can also be used in robocasting to fabricate a customized scaffold. The main drawback of CaP is their weak mechanical properties and brittle behaviour [11]. Due to these limitations, it is important to find a scaffold structure that optimizes the macroporosity while maximizing the apparent Young's modulus and ultimate strength.

1.4 μ-Computed Tomography

Due to the importance of the morphology of the scaffold, it is important to be able to determine the structure precisely. Micro-computed tomography (μCT) provides an exact image sequence of the actual structure. Moreover, μCT is a non-destructive technique, that allows scanning a scaffold and having the same specimen still available for further testing, for example mechanical testing. Other applications of μCT scanning are in vivo studies of bone or following the growth of native tissue within a scaffold and its degradation [14].

From the μCT image sequence, one can create a 3D reconstruction of the original structure and parameters, such as the pore density, the pore structure or other morphology parameters, can be evaluated [15]. Additionally, the 3D-reconstruction can also be used to build a finite element (FE) model of the scaffold. Figure 1.3 shows the process from the design file to the reconstruction of the fabricated scaffold.

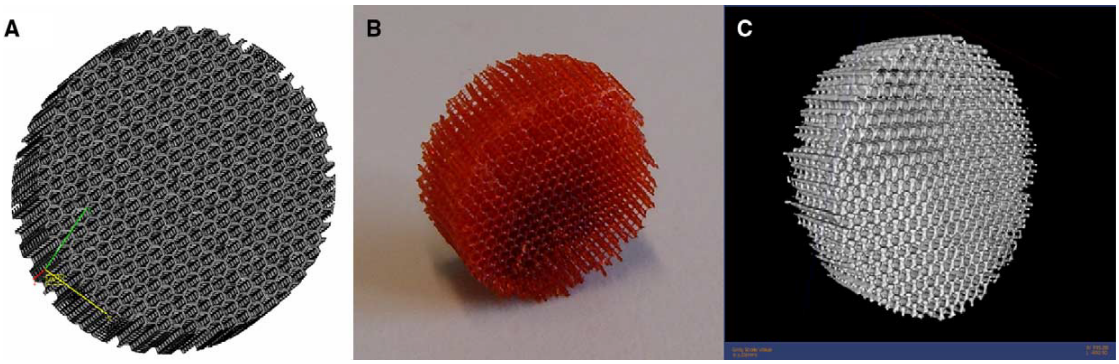

Figure 1.3: From Design File to Reconstruction - The figure on the left shows the design file of an architecture. The middle image shows the scaffold that was produced from the design file. The fabrication method used here was stereolithography. The image on the right shows a 3D reconstruction based on μCT images of the scaffold shown in the middle.[3]

1.5 Finite Element Modelling

FE modeling is a technique to tackle a problem, that can not be solved analytically. It is widely used in structural mechanics to analyse the design of various structures in regard of potential deformation but has also been generalized for other fields such as heat transfer or fluid dynamics. In this technique, the problem is devided into small parts for which the boundary value problem can be solved numerically. Reassembling all the parts and their individual solutions then gives the result for the whole problem. [16]

As mentioned earlier, the apparent mechanical properties of the scaffold have to match the properties of the native tissue. Creating such a scaffold from bulk material is fairly easy but becomes increasingly difficult when dealing with complex structures. Measuring the apparent properties of the scaffold and tuning the structure iteratively to reach appropriate levels (the Young's modulus of cortical bone is around 17 GPa and its ultimate strength up to 193 MPa [5]) is feasible, but very time- and money-consuming. On the other hand, reliably determining the local strains at a microscopic level which are transduced to the cells and act as mechanical stimuli is very cumbersome if not impossible. FE models excel at both. Once a design for a scaffold is introduced, a FE model with this design can be run while applying expected loading and boundary conditions. This results in both the strain distribution as well as the apparent properties of the scaffold. With these results, an easy comparison of different designs is possible. FE modeling therefore supports the goal of finding an optimal pattern for bone tissue engineering. [17] [18]

Basing the FE model on μCT images has some further advantages. First of all, it allows evaluating the properties of not only the designed pattern, but the actual scaffold that will finally be implanted[19]. It also facilitates finding defects from the fabrication process or other weak points in the scaffold and can identify possible fracture modes [20] [21].

1.6 Open Problems

The mechanical response, specifically the apparent stiffness and ultimate strength of the scaffolds used in bone tissue engineering, has not been exhaustively studied. Additionally, current studies mostly use simple architectures and do not fully exploit the capabilities of 3D-printing. Since the apparent properties of the scaffold are critical for a successful application in bone tissue engineering, it is required to have a tool, that supports the evaluation of different structures and thereby facilitates the design of scaffolds that combine a high porosity with suitable apparent properties.

[3] Image source: [7]

Chapter 2

Objective

The goal of this project was to set up a FE model simulation for the complete compression process of 3D-printed scaffolds. Such a simulation has to model both the linear elastic part of the deformation under compressive strain as well as the fracture of the scaffold. Additionally, this simulation also has to determine the stress and strain values at local areas of the scaffold.

In order to achieve this objective, two separate projects were set up:

Project I

In Project I, the simulation process was set up. The design of this simulation process also included comparing four types of elements and two different failure criteria. The methods and results of these studies are presented in Section 4.

Project II

In Project II, the mechanical performance of three different robocasted designs was compared. At the same time, the data was used to validate the simulation process. Section 5 presents the methods and results that were obtained.

Chapter 3

Finite Element Model and Failure Simulation

3.1 Simulation Process

The whole simulation process of the compression test consists of several main steps. It is illustrated in Figure 3.1. Before the actual simulation can be started, the data (i.e. the μCT images or the STL-file) must be processed and the parameters must be set accordingly. This is explained in more detail in Section 3.1.1. Once this is done, the simulation can be started as a script in Matlab. From the prepared data, this script creates a mesh as described in Section 3.1.2. With the mesh of the scaffold and the desired compression step, an input file can be written that includes all the required data for the FE model. As described in Section 3.1.3, this input file is handed over to Abaqus and the FE model is run. After successful completion of the calculation, the Matlab script reads in the computed stress and strain values and checks which elements failed in this step by the algorithm described in Section 3.1.4. It then writes a new input file with the next compression step and the adapted mesh and starts another FE model. Those steps are repeated until all the compression steps are calculated. When all the steps are finished, the data can be analysed.

The following sections describe each single step in more details.

3.1.1 Preparation

The initial input for the simulation is the 3D computational reconstruction of the scaffold. In the case of this study, it was provided either from μCT images of robocasted scaffolds, or directly from the design files used to print the scaffolds.

The images resulting from μCT scanning typically are grey-scale. Figure 3.2a shows the grey-scale μCT image of one slice of the scaffold. To avoid problems in the meshing algorithm where binary images are required, the grey-scale images first have to be converted to black and white, as seen in Figure 3.2b. Depending on the desired density of the mesh, the resolution might have to be adapted as well.

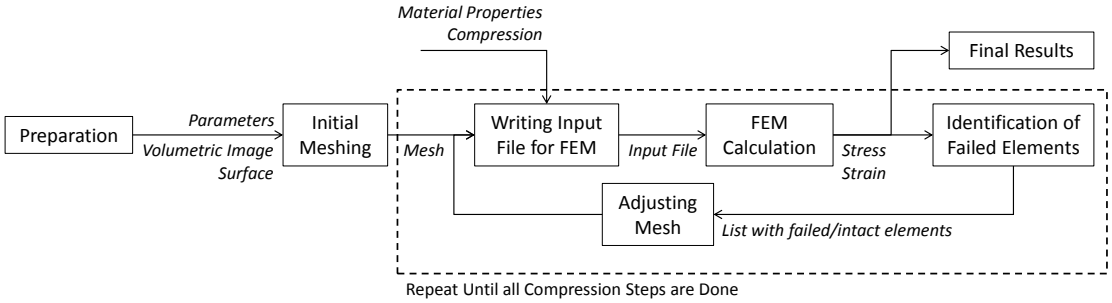

Figure 3.1: Diagram of Simulation Process - This diagram illustrates the simulation process.

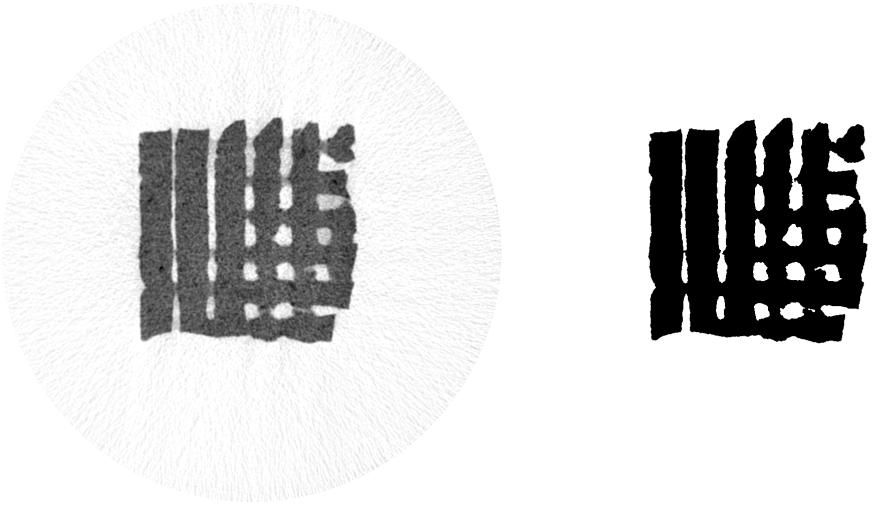

(a) Original μCT image in grey-scale. **(b)** Processed μCT image in binary.

Figure 3.2: The image on the left shows the original grey-scale μCT image and the image on the right is the same image converted to black and white. The resolution of both images is 14.95 µm.

Design files used for robocasting are usually STL-files. STL is an abbreviation of Stereolithography. Such a design file describes the surface of a given structure and can be created by various different Computer Aided Design (CAD) softwares.

Several parameters for the simulation process, most importantly the desired element type for the mesh, the material properties and the failure criterion, can then be set. For the simulation based on μCT images, the full range of different element types, i.e. both tetrahedrons and hexahedrons, can be used, while for the STL-based simulations only tetrahedrons are available.

3.1.2 Meshing

Based on the given input files, the Matlab script generates a mesh. There are currently four different mesh types implemented: linear tetrahedrons (four nodes), quadratic tetrahedrons (ten nodes), linear hexahedrons (eight nodes) and quadratic hexahedrons (20 nodes).

3.1.2.1 Tetrahedral Meshes

The linear tetrahedral meshes are created with the tool iso2mesh [22]. Both input types, STL-files and μCT image sequences, can be meshed with it. The size of the tetrahedrons can be scaled by a factor given to the toolbox but also depends on the resolution of the images or the STL-file. By changing these two parameters, a mesh with the desired density can be generated.

Quadratic tetrahedral meshes are based on a linear tetrahedral mesh, that was created as described above. The six additional nodes are then placed on the middle of each side of every element. Figure 3.3 shows the structure of the linear (4-node) tetrahedrons on the left and of the quadratic (10-node) tetrahedrons on the right.

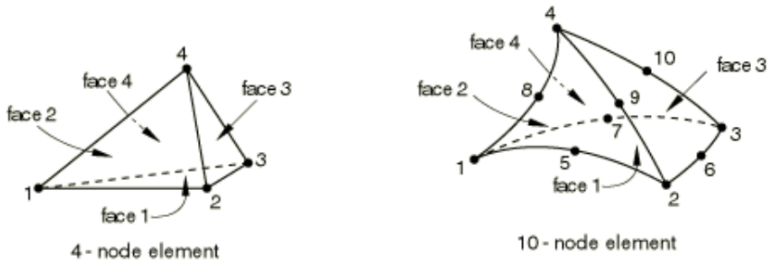

Figure 3.3: Structure of Tetrahedrons - Structure and node numbering of a linear tetrahedron with four nodes on the left and a quadratic tetrahedron with ten nodes on the right.[4]

[4]Image source: Abaqus User Manual 6.12

3.1.2.2 Hexahedral Meshes

The linear hexahedral meshes are generated using the direct voxel method which converts each pixel that represents part of the matter to an element of the mesh. This leads to the fact, that the hexahedron sizes are directly linked to the pixel sizes and therefore the resolution of the image sequence given as an input. Another consequence of this approach is that only μCT image sequences can be processed and it is not applicable for STL-files without further modifications.

Just like the quadratic tetrahedral meshes, the quadratic hexahedral meshes are based on their linear counterparts as well and the extra nodes are added in the middle of each side of every element.

Figure 3.4 shows the structure of the linear (8-node) hexahedrons on the left and of the quadratic (20-node) hexahedron on the right.

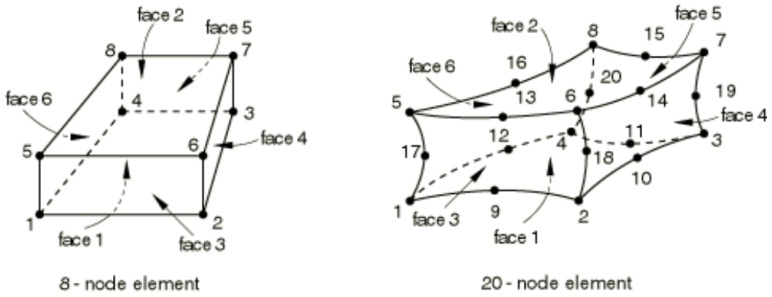

Figure 3.4: Structure of Hexahedrons - Structure and node numbering of a linear hexahedron with eight nodes on the left and a quadratic hexahedron with 20 nodes on the right.[5]

3.1.3 Finite Element Model

After the mesh is successfully created, an input file for the FE model calculation is written. This input file includes all nodes and all elements of the mesh, the boundary conditions, the applied displacement and the Young's modulus of the material. For all the models in this report, the boundary conditions and the displacement were set as follows:

- Top Nodes
  The nodes on the upper surface of the mesh were subjected to the desired compression in the z-direction, but could freely move along the x- and y-direction.
- Bottom Nodes
  The nodes on the lower surface were fixed in the z-direction, but could freely move along the x- and y-direction.

[5]Image source: Abaqus User Manual 6.12

- Wall Nodes
  The nodes on the outer surfaces of the mesh could move freely in all directions.

Figure 3.5 illustrates the applied boundary conditions in 2D, the extension to 3D is left to the imagination of the reader.

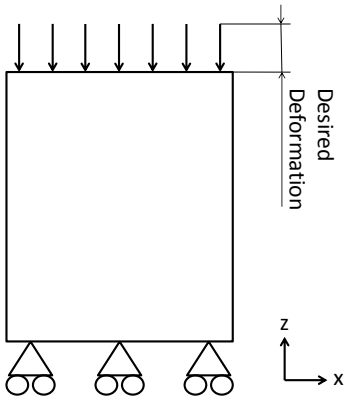

Figure 3.5: Applied Boundary Conditions in the FE model - Conceptual 2D illustration of the applied boundary conditions for the FE models used in this study.

This input file, containing the required data, is handed over to Abaqus which runs the FE model according to the given data. For the purpose of this study, a linear elastic model is used.

The results of the FE model calculation, including the stress and strain distributions, the displacements and the reaction forces at the boundary nodes, are written in a text file, which can be read by the Matlab script.

3.1.4 Application of Failure Criterion

The results from the FE model calculation are then read by the Matlab script, with the goal to determine if the equivalent stress in any element has exceeded the ultimate strength of the material and to mark these elements as broken. There exists a variety of different criteria to calculate the equivalent stress σ_v from the Cauchy stress tensor of each integration point. One of the most widely used is the von Mises criterion, described in section 3.1.4.1. Another possibility is the Rankine criterion which is mainly applicable for brittle materials, presented in section 3.1.4.2.

To simulate the failure of single elements and finally the fracture of the whole structure the so-called *kill element* approach is used [23]. In this method, those elements are marked as failed, that exceed their ultimate strength

$$\sigma_v \geq \sigma_u \tag{3.1}$$

where σ_u is the ultimate strength of the material. These broken elements are then assigned a Young's modulus that is non-zero but small enough so that these elements do not significantly contribute to the strength of the structure anymore. [23]

According to the used criterion, the elements are divided in one set that contains the intact elements and another set with the failed elements. Each of these two sets has its own material properties and is used for the FE model simulation of the next compression step.

3.1.4.1 Von Mises Criterion

The von Mises criterion is one of the most famous methods to calculate equivalent stresses. It is based on the distortion energy and therefore best applies to ductile materials. Nevertheless it is often used for different materials as well.

The von Mises stress can be calculated from the Cauchy stress tensor components as

$$\sigma_v^2 = \frac{1}{2} * ((\sigma_{xx} - \sigma_{yy})^2 + (\sigma_{yy} - \sigma_{zz})^2 + (\sigma_{zz} - \sigma_{xx})^2 + 6 * (\sigma_{xy}^2 + \sigma_{yz}^2 + \sigma_{xz}^2) \tag{3.2}$$

Assuming that the principle stresses are given, equation 3.2 can be rewritten as

$$\sigma_v = \sqrt{\frac{1}{2} * ((\sigma_1 - \sigma_2)^2 + (\sigma_2 - \sigma_3)^2 + (\sigma_3 - \sigma_1)^2)} \tag{3.3}$$

where $\sigma_1, \sigma_2, \sigma_3$ are the three principle stresses.

3.1.4.2 Rankine Criterion

The Rankine criterion, also know as Maximum Principle Stress Theory is a simple approach that allows for a quick calculation of element failure. It states that an element fails, when the equivalent stress exceeds the ultimate strength, where the equivalent stress is simply calculated as the maximum principle stress:

$$\sigma_v = \sigma_1 \tag{3.4}$$

where σ_1 is the maximum principle stress.

Despite the simplicity of this methods, it results in good predictions for brittle materials.

3.1.5 Analysis of Final Results

Once all the compression steps are simulated, the final force-displacement curve can be drawn in order to compare the simulation results to the experimental data. For this purpose, the nodes at the top surface of the scaffold are considered.

Since the simulation process is based on incremental steps, the result of a single compression step is only the incremental reaction force IRF. At the compression step

m, the reaction force RF of node n is therefore the sum over all IRF of the previous compression steps

$$RF_{step\ m,\ node\ n} = \sum_{i=1}^{m} IRF_{node\ n,\ step\ i} \tag{3.5}$$

To end up with the total (apparent) reaction force TRF of the compression step m, one has to sum over every node that belongs to an intact element

$$TRF_{step\ m} = \sum_{j=1}^{nmb\ intact\ nodes} RF_{step\ m,\ node\ j} \tag{3.6}$$

From the force-displacement curve, the apparent material properties of the scaffold can then be calculated.

3.2 Hardware

The simulations conducted for this project were all performed on a laptop with an Intel Core i7-2630QM CPU and 8 GB of random access memory (RAM).

3.3 Software

To simulate the finite element models, the software Simulia Abaqus in the version 6.12 from the company Dassault Systemes was used.

Matlab was used to create meshes, analyse the output of the FE model simulations and to visualize results.

Tetrahedral meshes were created with the iso2mesh toolbox, which is licensed under a public license [22]. This software is a multifunctional toolbox, that can create 3D tetrahedral meshes from different sources such as surfaces, 3D binary and gray-scale volumetric images. Additionally, it also allows to process and adjust given meshes. For these purposes, it makes use of the CGAL utility [24] and the TetGen program [25]. CGAL is the abbreviation for Computational Geometry Algorithms Library. As its name suggests, it is a project that gives access to data structures and geometric algorithms. The volume mesh generation is just one example of its many functionalities. TetGen is a mesh generator creating a tetrahedral mesh from any 3D surface by Delauny triangulation.

ImageJ was used to prepare the μCT images for the simulation process [26]. The applied modifications are described in section 3.1.1.

Chapter 4

Project I: Set Up of the Simulation and Comparison of Failure Criteria

4.1 Materials

The dataset used in Project I was originally produced and published by Maazouz [27]. Briefly, a mixture of alpha tricalcium phosphate (α-TCP) and Gelatine was 3D-printed into a cuboid consisting of parallel filaments rotated by 90° at each new layer. Figure 4.1 shows an image of the specimen, recreated from μCT images. This specimen was then subjected to a compression test, applied stepwise. After each compression step, a μCT scan with a resolution of 14.95 µm was conducted. This way, a dataset was obtained that includes both the μCT images at each compression step and the corresponding force and displacement values. The detailed informations and images were kindly provided for this project.

4.2 FE Model Details

The FE model was set up as described in Section 3.1.3. The values for the displacement that was to be applied was ranging from 0.05 mm to 0.35 mm in 0.05 mm steps. The material properties, especially the Young's modulus, were unknown. Since the values for the total reaction force and the displacement were given though (see Figure 4.2), the Young's modulus used in the simulation was tuned so that the simulation with 4-node tetrahedrons and the Rankine Criteria matches the curve from Figure 4.2. This resulted in a Young's modulus of 208 MPa, an ultimate strength of 5.9 MPa and a poisson ration of 0.3. Those values were held constant for all the simulations in Project I.

[6] Image kindly provided by Yassine Maazouz

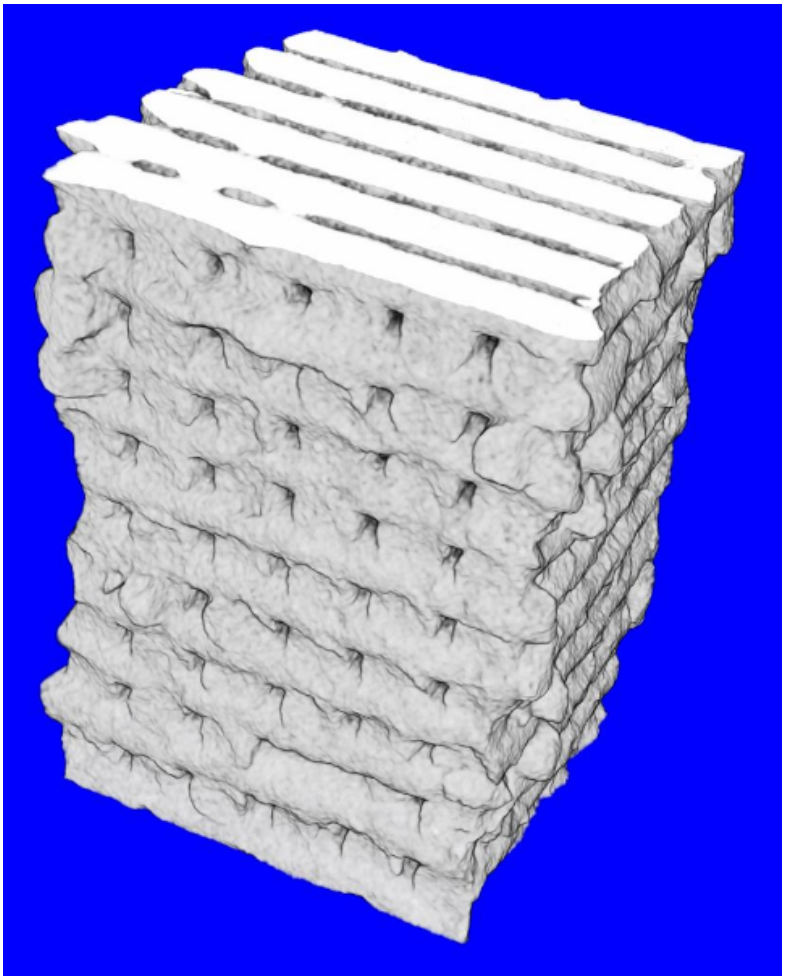

Figure 4.1: Scaffold of Project I - The specimen that was used for Project I, recreated from the μCT images.[6]

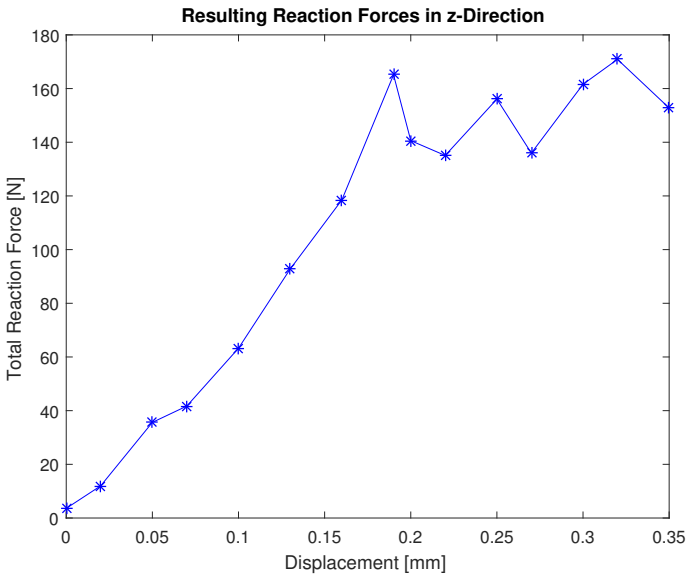

Figure 4.2: Reaction Forces from Compression Test - This figure shows the total apparent reaction force that was measured during the compression test of the scaffold.

4.3 Comparison of Tetrahedral to Hexahedral Meshes

When developing a FE model, one of the first questions that needs to be addressed is what element type to use. The two most popular types in the literature are tetrahedral elements and hexahedral elements. Using tetrahedrons with four nodes, one at each corner, leads to linear governing equations resulting in elements that are too stiff for many applications. To decrease the stiffness, an additional node can be inserted at every edge, creating a tetrahedron with ten nodes which is governed by quadratic equations. The same method can be applied to create hexahedrons with twenty instead of eight nodes. [28] [29] [30]

4.3.1 Methods

To evaluate the performance of each of those four element types, a set of three criteria was defined. The first criterion is the run time, defining the total duration it takes to calculate one compression step. Then the different element types are evaluated by the minimum number of elements that are needed to build up the shape defined by the μCT images in a recognizable manner. The last criterion is how well the whole simulated compression process approximates the measured stress-strain curve.

These four criteria are evaluated in the following sections on the simulation of the single dataset of Project I. All parameters of the simulation except for the used element type remained unchanged.

4.3.2 Results

4.3.2.1 Run Time

To compare the run time of the different element types, 14 FE models were run for each type. These 14 models included two different failure criteria with each seven compression steps. Figure 4.3 shows the statistics of around 14 models run for each element type. As expected, the 4-noded tetrahedrons are computationally very efficient. The median CPU-time to run one model takes only about 100 s. This efficiency is lost, when the six additional nodes are inserted to form 10-node tetrahedrons. With a median CPU-time of around 2600 s, the models with 10-node tetrahedrons are just slightly faster than the ones with 8-node hexahedrons which take around 2700 s. The 20-node hexahedrons were computationally so demanding, that it was not possible to run the models on the machine used in this project.

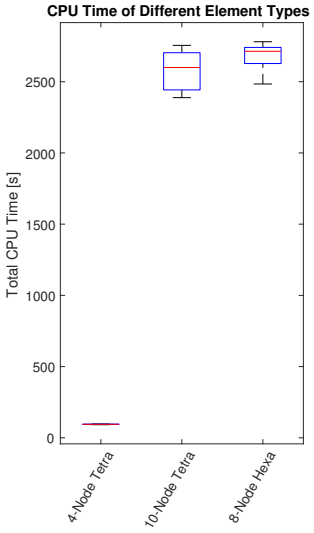

Figure 4.3: CPU-Time with Different Element Types - Shown are the boxplots of the three different element types. On the left, the boxplot for the 4-node tetrahedrons is plotted. Due to the scale of the y-axis, only the median is visible. In the middle, the results for the 10-node tetrahedrons and on the right, the ones for the 8-node hexahedrons are shown. The red line shows the median and the box includes 50 % of all values.

4.3.2.2 Shape Accuracy

Figure 4.4a shows the tetrahedral mesh that was created based on the μCT images of the scaffold. Figure 4.4b shows the corresponding hexahedral mesh. Both meshes consist of approximately 350 000 elements. Since the 10-node tetrahedral mesh is based on the 4-node tetrahedral mesh, their appearance is equivalent and hence only the 4-node

tetrahedral mesh is shown. The same applies for the 20-node hexahedral mesh.

It is immediately visible that the tetrahedral mesh is clearly superior in modelling the surface of the original structure. Not only do the curved edges better reflect the original shape but the tetrahedral mesh also holds more details, especially visible for the pores and holes. Since the macroporosity is the core of this study, this is a major advantage of the tetrahdral mesh over the hexahedral mesh

Due to the fact that the number of elements depends on the resolution of the input images, the images used for the hexahedral mesh had to be downsampled by a factor of two compared to the ones used for the tetrahedral mesh. This supports the assumption that the tetrahedrons are better suited to create a mesh that is as close to the original structure of the scaffold as possible

4.3.2.3 Compression Behaviour

In this section, the behaviour of the elements when subjected to a compression is investigated. For this purpose, the same simulation was run with the three different element types. The compression steps with their corresponding reaction forces are shown in Figure 4.5.

As expected, the 4-node tetrahedrons are the stiffest of the three investigated element types. The 10-node tetrahedrons and the hexahedrons on the other hand have a very similar shape, with the 10-node tetrahedrons slightly stiffer than the hexahedrons. The similarity of these two curves confirms that the results of the FE models converge to the correct solution.

4.3.3 Discussion

The main advantage of the 4-node hexahedrons is the computational efficiency. Since a runtime of around 2600 s is still acceptable the 10-node tetrahedrons or the hexahedrons are preferable due to their behaviour in the compression test.

While the hexahedrons guarantee a problem-free meshing of any structure that is given as an input, the 10-node tetrahedrons are clearly superior in reproducing the original structure of the scaffold. So even though the 10-node tetrahedrons are not the distinct leader in any of the evaluated categories, they are chosen for all the further simulations because they offer the best compromise between shape accuracy, computation time and approximation of the solution.

4.4 Comparison of Yield Criteria

The behaviour of the scaffold in the compression test was composed of a linear elastic part at the beginning that is captured well in the FE model. Once the applied stress exceeds a threshold though, a brittle fracture appears. To model the failure, two different yield criteria have been implemented. As one of the most popular yield criteria, the von Mises criteria was integrated in the algorithm. The second option is the Rankine criteria, that is said to fit mostly brittle materials.

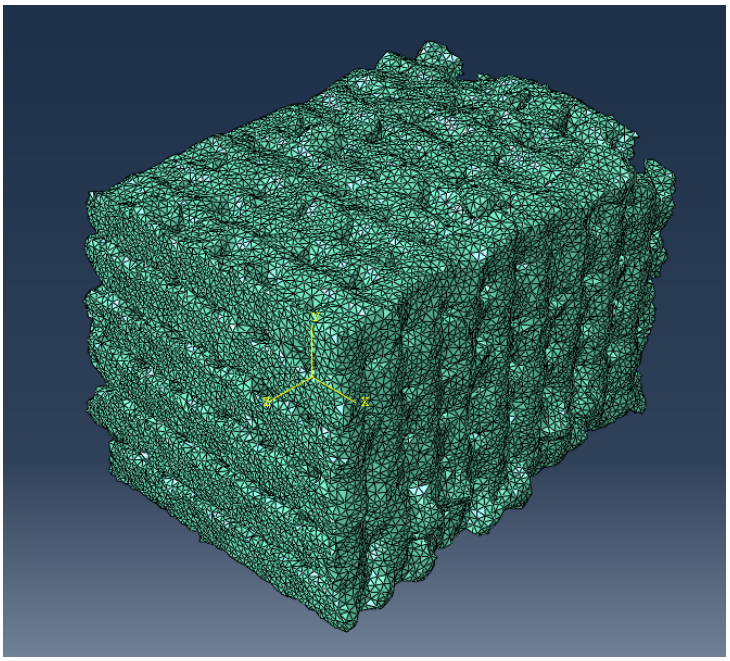

(a) Scaffold meshed with tetrahedrons

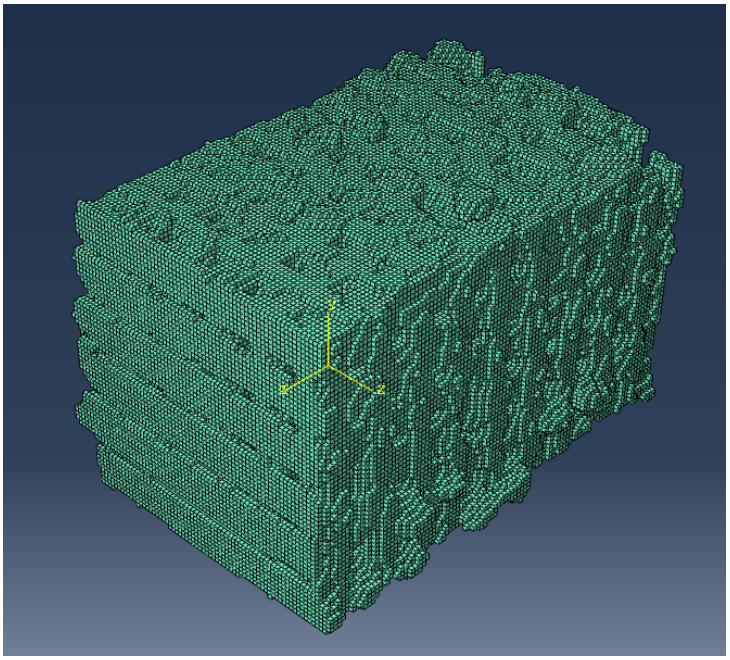

(b) Scaffold meshed with hexahedrons

Figure 4.4: Comparison of different meshes. Both the tetrahedral mesh and the hexahedral mesh are composed of around 350 000 elements.

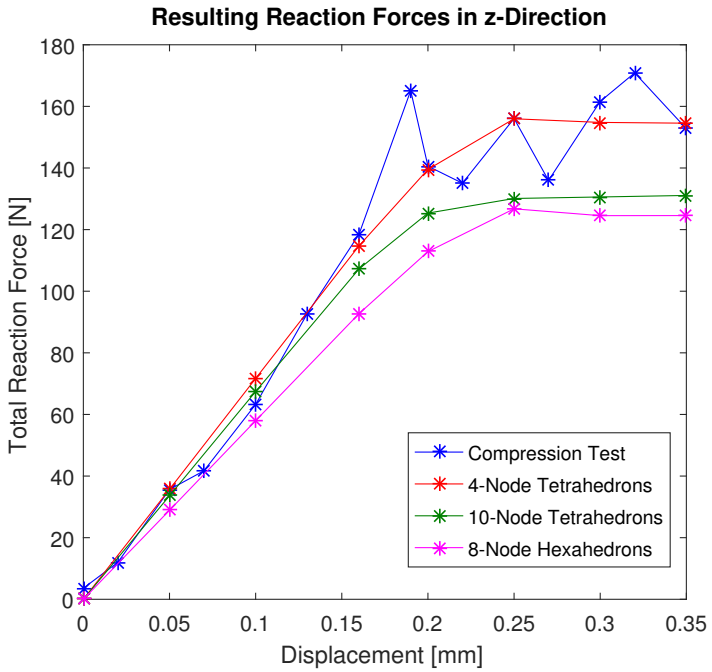

Figure 4.5: Compression Behaviour - This graph plots the compression values on the x-axis and the total reaction force on the y-axis. The blue curve represents the data from the compression test, the red, green and pink curves show the simulation results with 4-node tetrahedrons, 10-node tetrahedrons and hexahedrons, respectively.

4.4.1 Methods

Each of the two implemented criteria is rated by their compression behaviour and by how well they manage to simulate the fracture. They are again evaluated on the single dataset of Project I and all the parameters of the simulation except for the yield criterion are held constant. Please note that these simulations are now run with 10-node tetrahedral elements as concluded in Section 4.3.

4.4.2 Results

4.4.2.1 Compression Behaviour

Figure 4.6 shows how the two different yield criteria performed in the simulation. During the linear elastic part of the model, i.e. up to a deformation of 0.16 mm, where no elements are failing, both yield criteria are identical. For higher deformations, more elements fail which leads to a smaller total reaction force for both yield criteria. The difference between the two criteria is so small however, that no preference can be drawn.

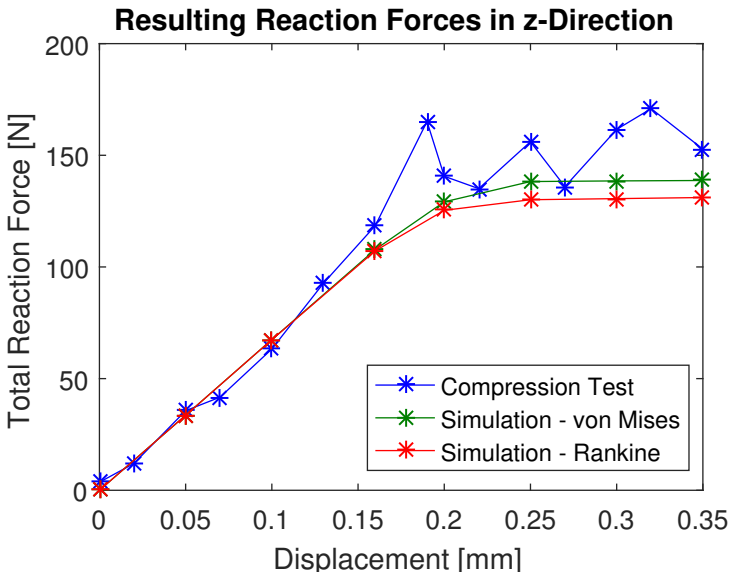

Figure 4.6: Compression Behaviour - This graph plots the compression values on the x-axis and the total reaction force on the y-axis. The blue curve represents the data from the compression test and the red and the green curves show the simulation results with the Rankine criterion and the von Mises criterion, respectively.

4.4.2.2 Matching of Fracture Origin

The CaP used to produce the scaffold of Project I resulted in a brittle material. This lead to a fracture determined by crack propagation, shown in Figure 4.7. As it can be

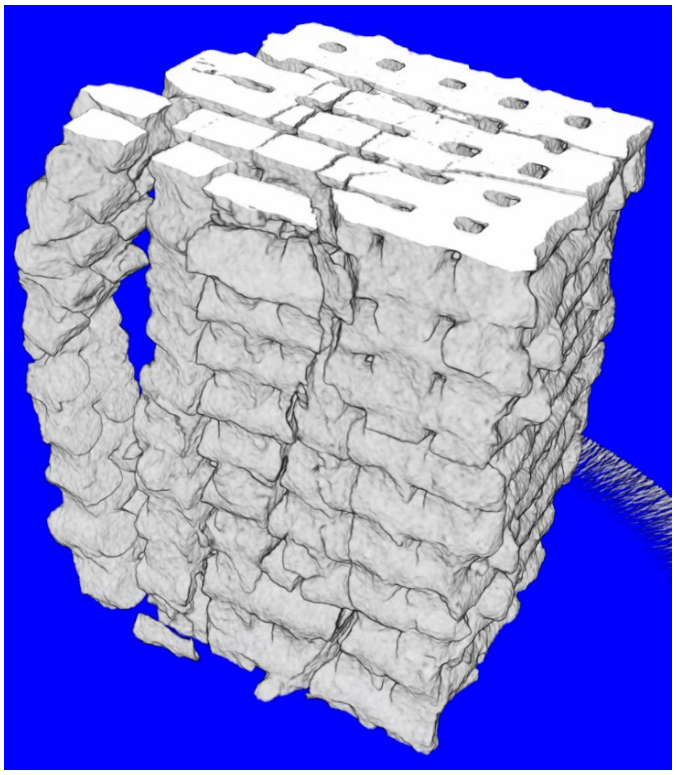

Figure 4.7: Fractured scaffold recreated from μCT images.[7]

seen in Figure 4.8b and Figure 4.8d none of the two yield critera manages to predict the fractures appearing in the scaffold appropriately. Since the simulation of a propagating crack is an unsolved problem, this was to be expected.

Nevertheless, both criteria allow to define weak points and possible origins of fractures within the structure. Figure 4.8a and Figure 4.8c, both very similar, show areas of failed elements, that overlap with the fractures occuring in the compression test of the real scaffold. These areas are marked in red. The Rankine criteria appears to predict those weak areas slightly better with a higher density of failed elements around the origin of the fracture in the real scaffold.

4.4.3 Discussion

Both yield criteria do not realise an appropriate simulation of the occurring fractures. This does not represent a major drawback, considering that for the scope of this simulation, how the scaffold fractures is not closely as important as at what point it does so. And unlike the prediction of the crack propagation, the simulation of the onset of the fracture is fairly successful with both yield criteria. With both criteria performing

[7] Image kindly provided by Yassine Maazouz.

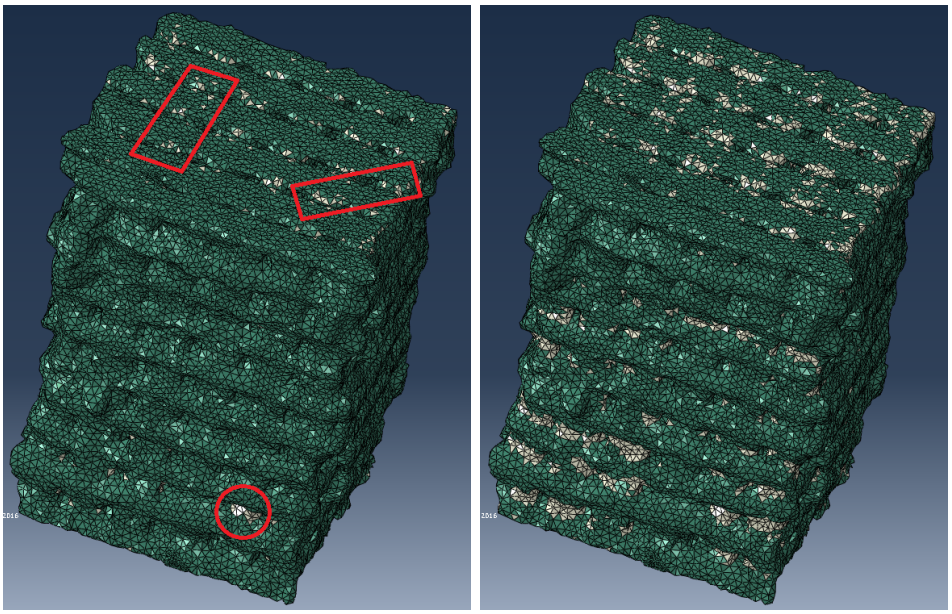

(a) Simulation with Rankine criterion and a compression of 0.16 mm.

(b) Simulation with Rankine criterion and a compression of 0.2 mm.

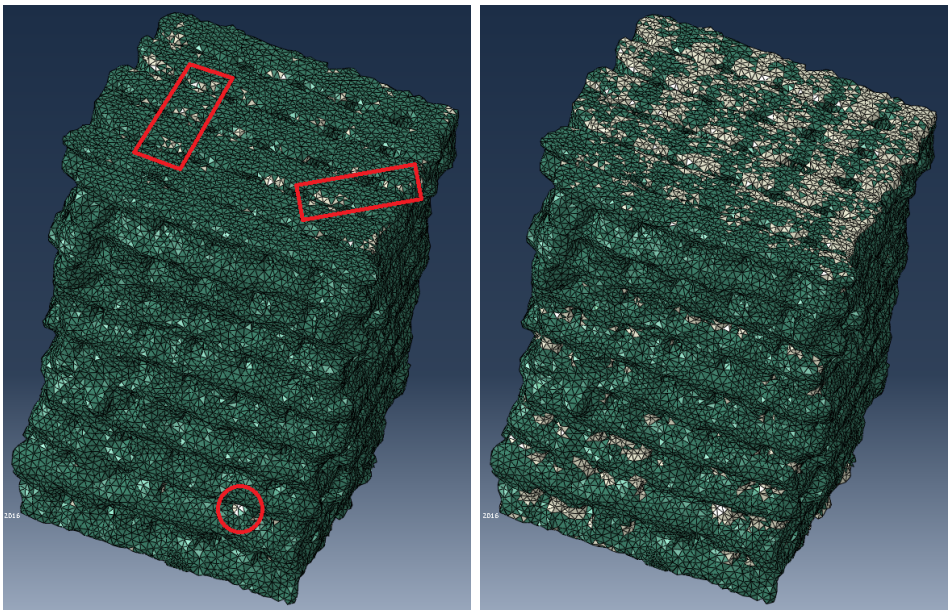

(c) Simulation with von Mises criterion and a compression of 0.16 mm.

(d) Simulation with von Mises criterion and a compression of 0.2 mm.

Figure 4.8: Fracture Prediction with Different Yield Criteria - The images in the top row and in the bottom row show the fracture prediction with the Rankine and the von Mises criterion, respectively. The red marks show failed elements, that overlap with the actual fractures.

equally well, the Rankine criterion was chosen for the further simulations simply because it is generally assumed to be the best fit for brittle materials.

Chapter 5

Project II: Comparison Between Three Different Patterns of Robocasted Scaffolds

5.1 Materials

The second dataset was taken from an internal study performed by González [31]. The objective of that study was to compare how different 3D-printing patterns perform under compression. For that purpose, three different patterns were designed:

- **Orthogonal**
  Parallel strands make up one layer. The direction of the strands is rotated by 90° from layer to layer.

- **Orthogonal Rotated**
  Parallel strands make up one layer. The direction of the strands is rotated by 45° from layer to layer.

- **Honeycomb**
  Each layer is printed in a honeycomb pattern. The layers are rotated by 180°.

The different structures are illustrated in Figure 5.1. STL-files, describing those designs, were then created by CAD. Those STL-files were used to fabricate several specimen of each pattern. The material that was used to produce them was a combination of α-TCP and Pluronics F127 (Sigma Aldrich P2443). One of these specimens was analysed in a μCT scanner and the rest of them were subject to a compression test.

[8] Image from the report of Borja González

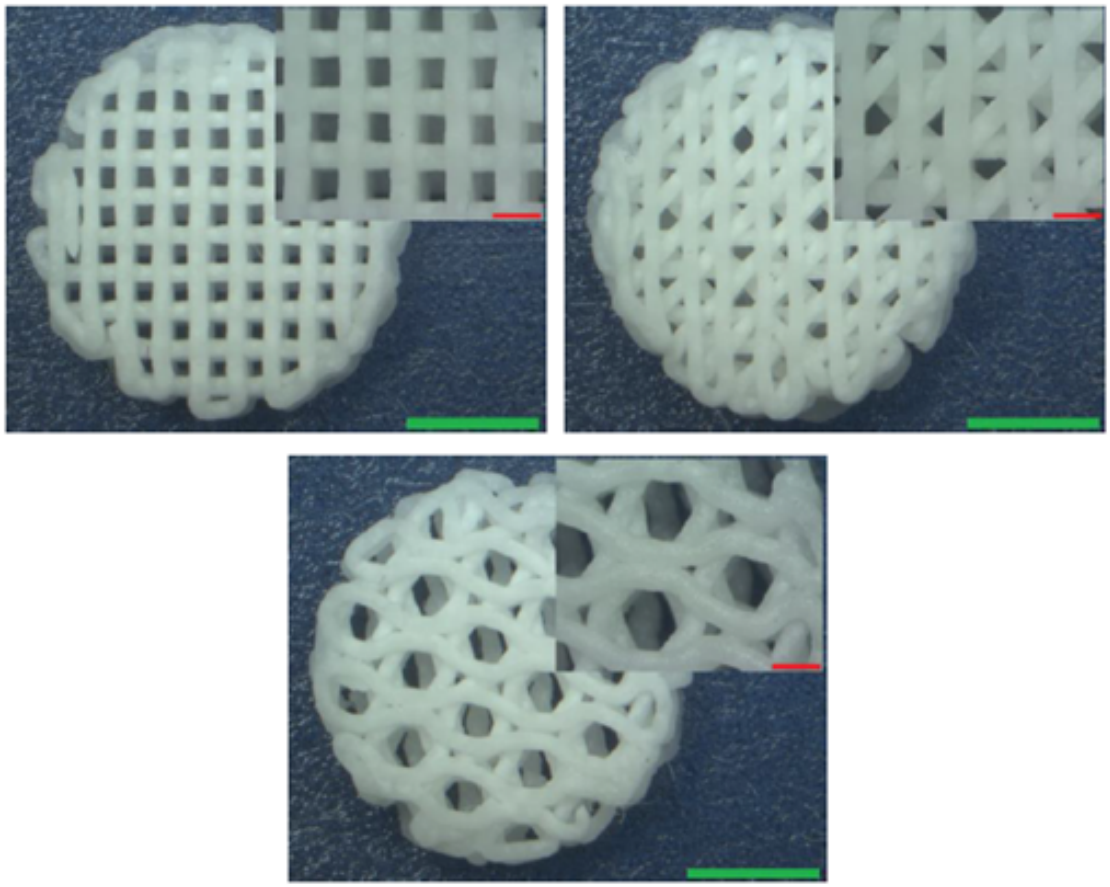

Figure 5.1: Scaffolds of Project II - The structure of the Orthogonal scaffold is shown in the top row on the left, the Orthogonal Rotated pattern on the top right and the Honeycomb pattern on the bottom. The green bar corresponds to 2 mm and the red bar in the detail to 500 µm.[8]

Pattern	Number of Specimen Used for Testing	Number of Specimen Used for μCT
Bulk Material	17	0
Orthogonal (O)	14	1
Orthogonal Rotated (OR)	14	1
Honeycomb (HC)	21	1

Table 5.1: This table shows the how many specimen of Project II were used for either the mechanical testing or for a μCT scan.

5.2 Processing and Evaluation of Input Data

In addition to the data that was provided, the properties of the material that was used to create the patterned scaffolds have to be known. For this purpose, cylinders were produced from the same material and tested with the same mechanical testing protocol as the other scaffolds.

Table 5.1 shows how many specimen were used in the compression tests and for the μCT scanning. It is important to note, that unlike in Project I, different specimen were used for mechanical testing and for μCT scanning. Another difference is that the specimen analysed in μCT was not subjected to compression, as it was in Project I.

Since several specimen were tested, statistics have to be applied to the original data to be able to reliably calculate the expected apparent stiffness and ultimate strength of the specimen. Figure 5.2 shows the original compression data of the different patterns as it was measured.

To reduce the noise of the compression curves, the data was filtered with a moving average filter over ten data points. Additionally, the onset of the curves varies due to the adjustment and alignment of the piston at the beginning of the compression test. To adjust for this variation, the curves were shifted along the x-axis so that all curves cross the 4 N mark at the same point. Figure 5.3 shows the filtered and shifted curves.

Averaging over all the specimen and calculating the standard deviation resulted in the curves shown in Figure 5.4. The average was chosen over the median due to the smoothness of the resulting curves. Since no clear outlier is apparent in Figure 5.3, this does not lead to statistical problems.

From the compression, the averaged reaction force and with the specifications of the used specimen, the apparent stress and strain can be calculated. This data is illustrated in Figure 5.5 for the three different patterns and the bulk material. Once the stress and strain values are calculated, it is easy to obtain the required material properties, i.e. the ultimate strength and the Young's modulus, from them. The Young's modulus is indicated in Figure 5.5 in black. The values are shown in Table 5.2 together with the ultimate strength of each pattern.

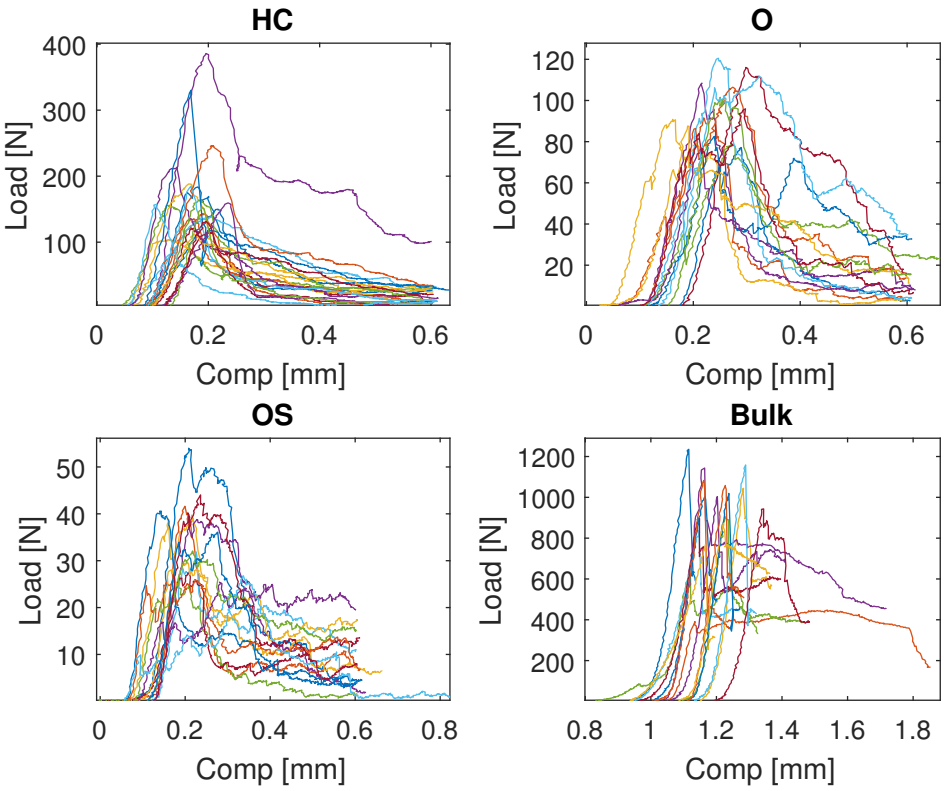

Figure 5.2: Original Compression Data - This figure shows the results of the compression test of the Honeycomb pattern on the top left, of the Orthogonal pattern on the top right, of the Orthogonal Rotated on the bottom left and of the bulk material on the bottom right.

Pattern	Young's Modulus [MPa]	Ultimate Strength [MPa]
Bulk Material	3610	27
Orthogonal (O)	420	3.1
Orthogonal Rotated (OR)	213	1.1
Honeycomb (HC)	1090	5.6

Table 5.2: This table shows the apparent Young's modulus and ultimate strength of each pattern and the material properties of the bulk material.

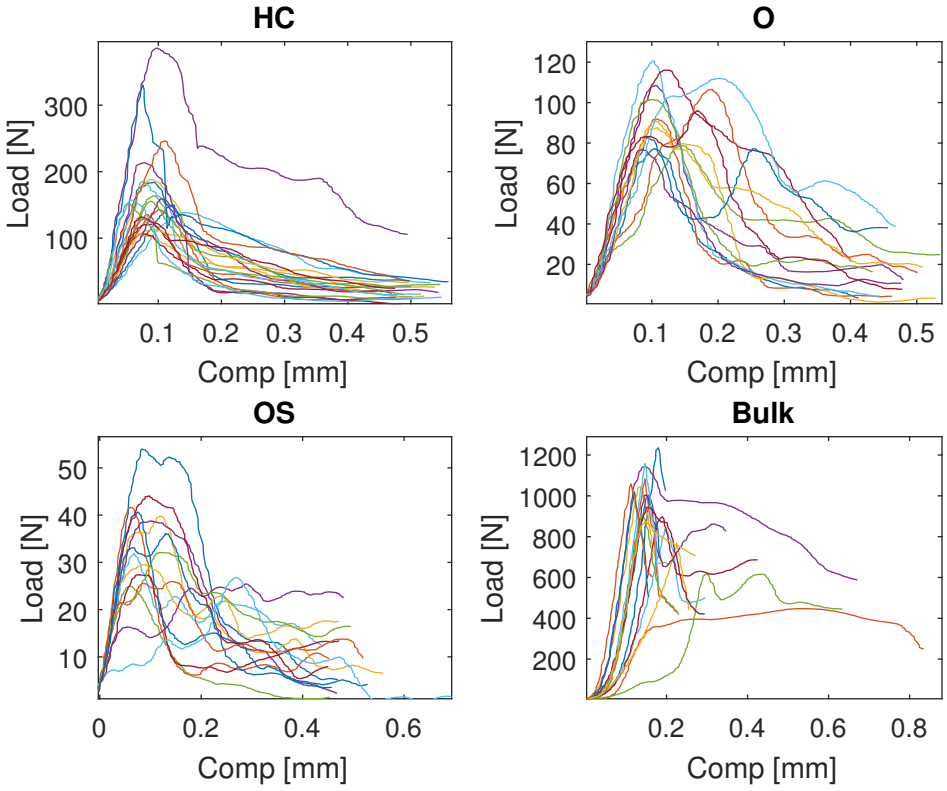

Figure 5.3: Filtered Data - This figure shows the processed data of Honeycomb (HC), Orthogonal(O), Orthogonal Rotated (OR) and bulk pattern.

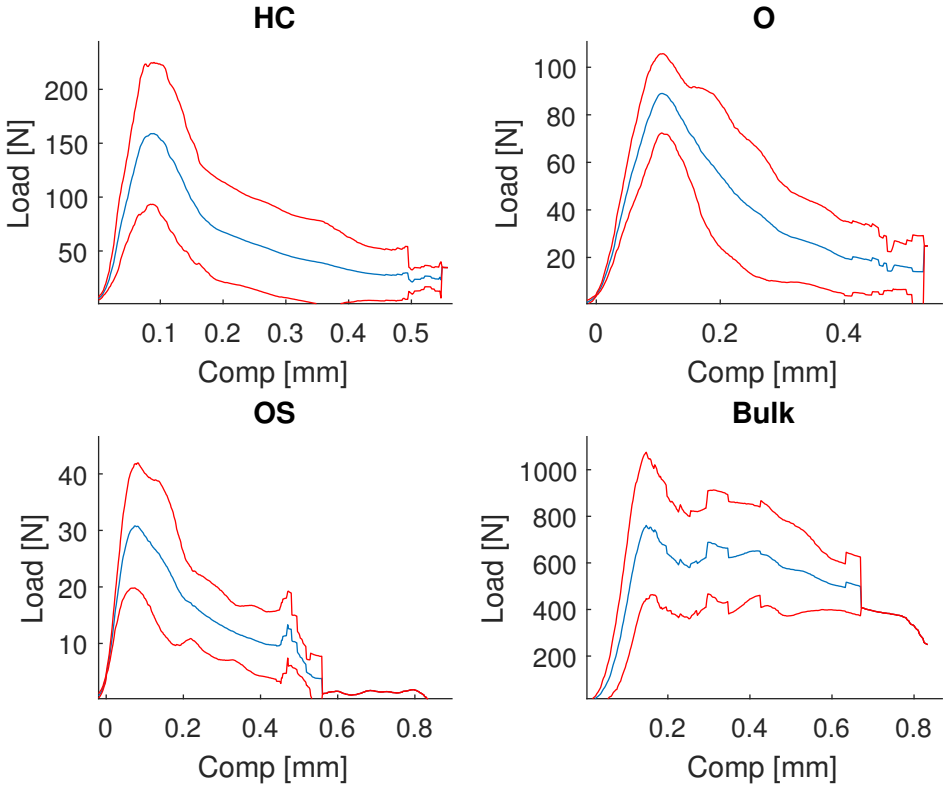

Figure 5.4: Averaged Data - This figure shows the statistically evaluated data from Figure 5.3. The blue line shows the average over all the specimen of each pattern and the red curves are the average plus and minus the standard deviation.

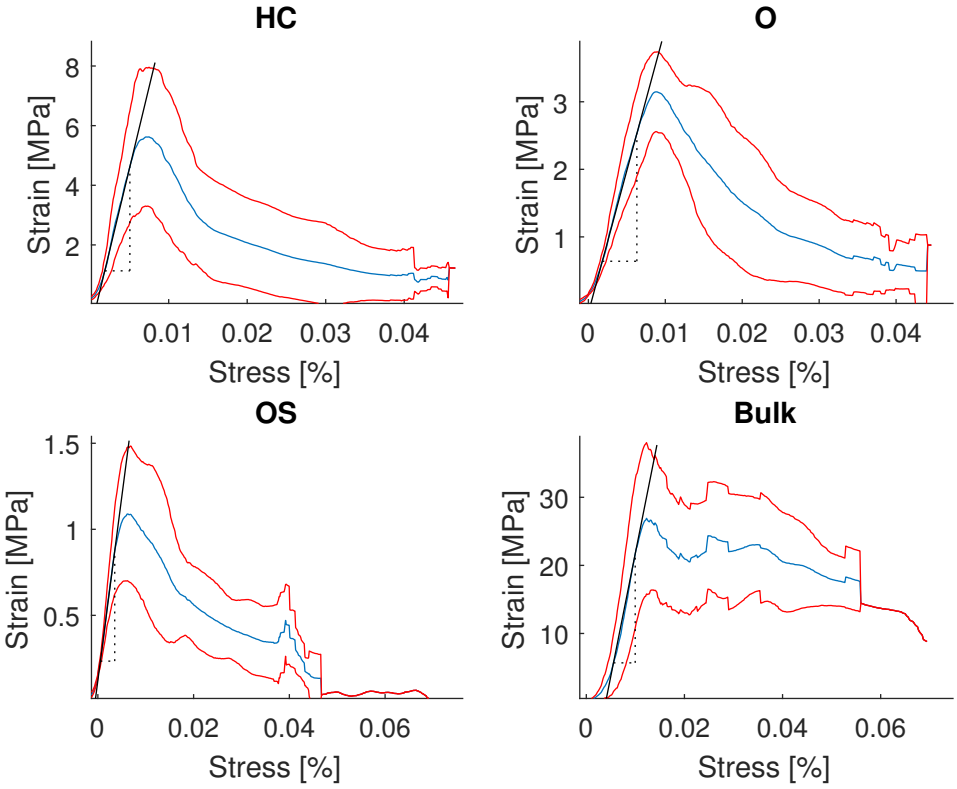

Figure 5.5: Stress and Strain of the four different patterns - The data is shown for the Honeycomb pattern on the top left, the Orthogonal pattern on the top left, the Orthogonal Rotated pattern on the bottom left and the bulk material on the bottom right. Please note the different scales on the y-axis. In all four graphs, the blue line shows the average apparent stress and the red curves illustrate the average plus and minus the standard deviation. The black lines additionally indicate the Young's modulus.

5.3 Simulation of Bulk Material

With the simulation procedure established in Section 4 and the material properties known from Section 5.2, a first and simple test whether the simulation process is capable of delivering consistent results is to simulate the compression of the bulk material in the form of a simple cylinder. Due to a limited availability of the μCT-scanner, it was not possible to scan a bulk material cylinder. That is why, the simulation had to be based on the STL-file of the cylinder.

Figure 5.6 shows the results of this simulation in green and in red the averaged measured data. The linear elastic part of the simulation and the compression test are identical up to the yield point. At the yield point, a large part of the load bearing elements fail in the simulation, representing a brittle failure of the cylinder. The same behaviour can be observed for single specimen in Figure 5.2 on the bottom right. The red curve does not show the same behaviour due to the averaging over several specimen.

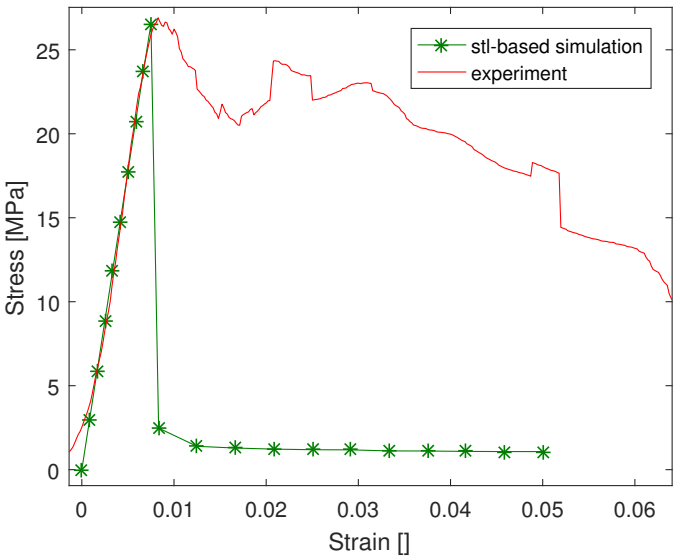

Figure 5.6: Simulation Results of Bulk Cylinder - This figure shows the average stress-strain curve as measured in the compression test for the bulk cylinder in red and in green the simulation results.

The results confirm, that the simulation procedure is capable of modeling the linear elastic part of the compression of a simple scaffold and predict its fracture point properly. The simulation of the failure of the model was more accurate than it could have been expected and supports the implementation of the failure algorithm.

Young's Modulus [MPa]			
Pattern	**Experiment**	**STL-Based Simulation**	**μCT Based Simulation**
Orthogonal	420	1447	1501
Orthogonal Rotated	213	1216	1938
Honeycomb	1090	1722	1882

Table 5.3: This table shows the apparent Young's modulus of each pattern as a result of the simulations along with the experimental data.

Ultimate Strength [MPa]			
Pattern	**Experiment**	**STL-Based Simulation**	**μCT Based Simulation**
Orthogonal	3.2	8.2	5.9
Orthogonal Rotated	1.1	7.5	9.7
Honeycomb	5.6	11	11

Table 5.4: This table shows the apparent ultimate strength of each pattern as a result from the simulation along with the experimental data.

5.4 Simulation of Patterned Scaffolds

Section 5.3 showed that the simulation procedure is able to model the compression of a cylinder well. This confirms, that the simulation can also be applied to the more complex structures. Therefore, in this section, the predicted mechanical behaviour of the patterned scaffolds will be evaluated.

5.4.1 Simulation Results

For each of the three different patterns, the simulation was run twice. Once the FE model was based on the STL-file and once it was based on the μCT images. For all the simulations, the same bulk material properties were used. The results of these simulations are shown in Figure 5.7.

The first thing that can be seen is that all simulations overestimate both the Young's modulus and the ultimate strength of the patterned scaffolds. But even though the absolute values from the simulation differ significantly from the ones that were measured, the overall ranking shown in Table 5.2 can be preserved with the STL-based simulations. The Honeycomb pattern, that proved to be strongest and stiffest in the testing, is also the strongest in the simulation and the Orthogonal Rotated pattern, that was the weakest and least stiff in the testing, is also the weakest in the simulation. The μCT-based simulations on the other hand fail to even result in the right ranking. The Young's modulus and the ultimate strength that result from the simulations are shown in Tables 5.3 and 5.4.

The second thing that can be noticed in the graphs is that the general shape of the

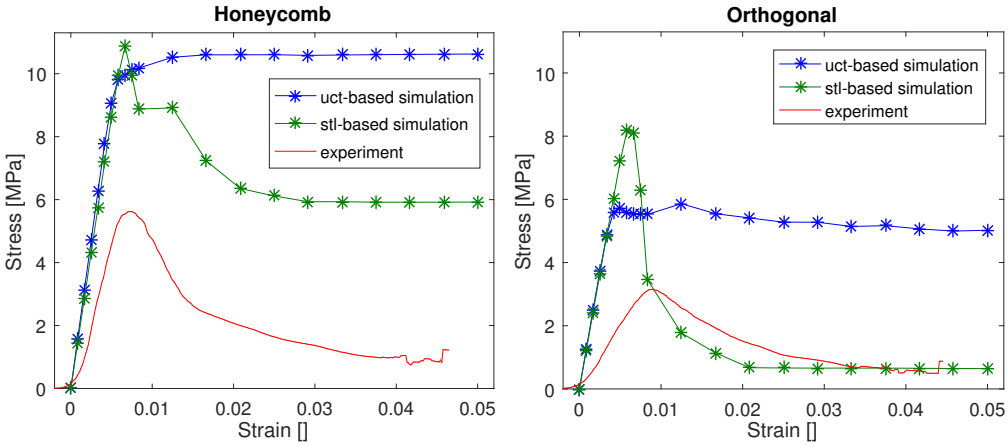

(a) Honeycomb pattern

(b) Orthogonal pattern

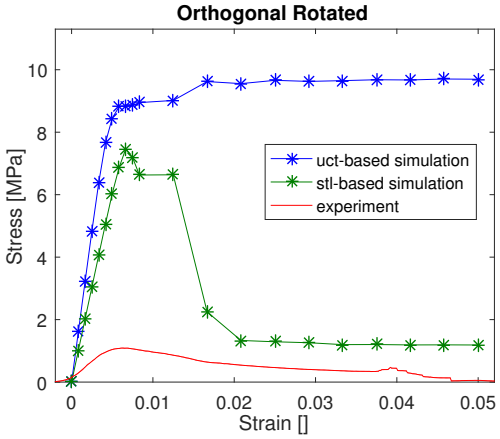

(c) Orhtogonal Rotated pattern

Figure 5.7: Simulation Results of Patterned Scaffolds - The graph on the top row shows the result of the Honeycomb structure, in the middle the results for the Orthogonal structure is illustrated and the bottom graph plots the results for the Orthogonal Rotated scaffold. In each of the graphs, the red line represents the average data from the compression tests, the blue line shows the simulation results with the model based on the μCT images and the green curve shows the results of the STL-based simulation.

STL-based simulations approximate the shape of the stress-strain curves from the testing reasonably well. Like the compression test, the simulation results in a linear elastic part at the beginning followed by a distinct peak. Once this peak is reached, a lot of elements fail, resulting in a sudden decrease of the apparent stress. This simulates well a brittle fracture. But again, the μCT-based simulations do not result in a peak but a platform instead, once the linear elastic part has finished.

5.4.2 Differences between STL-Based and μCT-Based Models

Section 5.4.1 showed that there is a significant difference between the STL-based and the μCT-based simulations. This section therefore attempts to identify possible sources of the differences. For this purpose the STL-based FE model is compared to the μCT-based model by the example of the Orthogonal pattern.

Figure 5.8 shows the two models based on the STL-file and the μCT images. It is immediately visible, that the STL-based model is a perfect recreation of the Orthogonal pattern. This was expected since the STL-file is the design file and if it was not the case it would indicate a problem in the meshing algorithm. The μCT-based model on the other hand includes many defects. Most obviously, single filaments are thicker than they are designed, resulting in smaller holes and pores. Under the assumption of perfect attachment between the filaments, this should result in higher apparent mechanical properties. However, the attachment can not be guaranteed to be perfect. It is very well possible, that certain layers are better attached than others, resulting in a different behaviour when subjected to compression.

Two other possible defects in the μCT-based models are shown in Figure 5.9. The image on the left shows that the model is not standing totally straigth but is tilted to the right. Since the compression is applied vertically, this influences the strength of the material. The source of this defect could either be a miss-alignment during the 3D-printing or during the μCT-scan.

Image 5.9b shows a cross section of the model. The filament orientation within the red circle is different from the orientation of the filaments outside of the red circle. This indicates that the filament were sagging during the 3D-printing process.

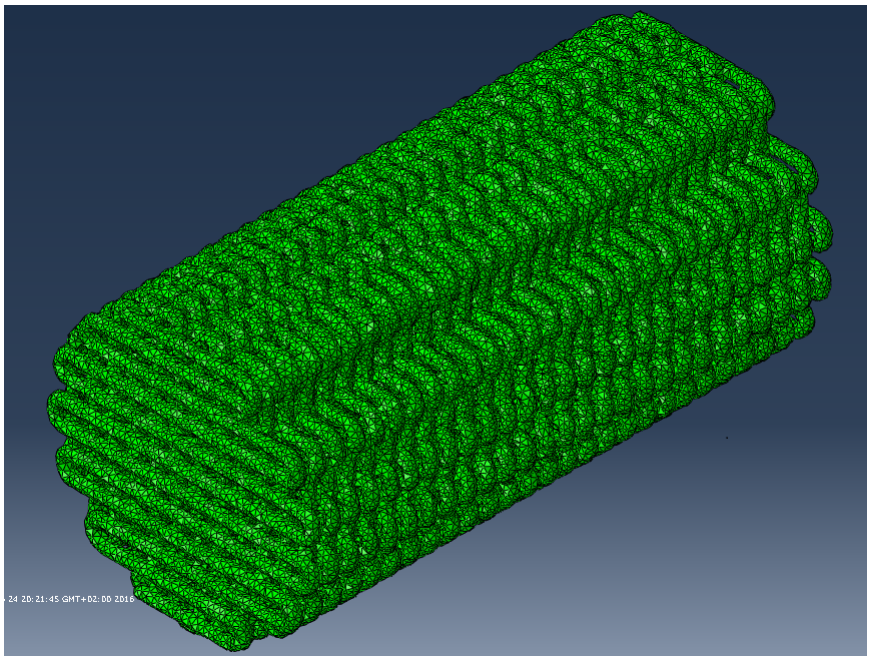

(a) STL-based FE model

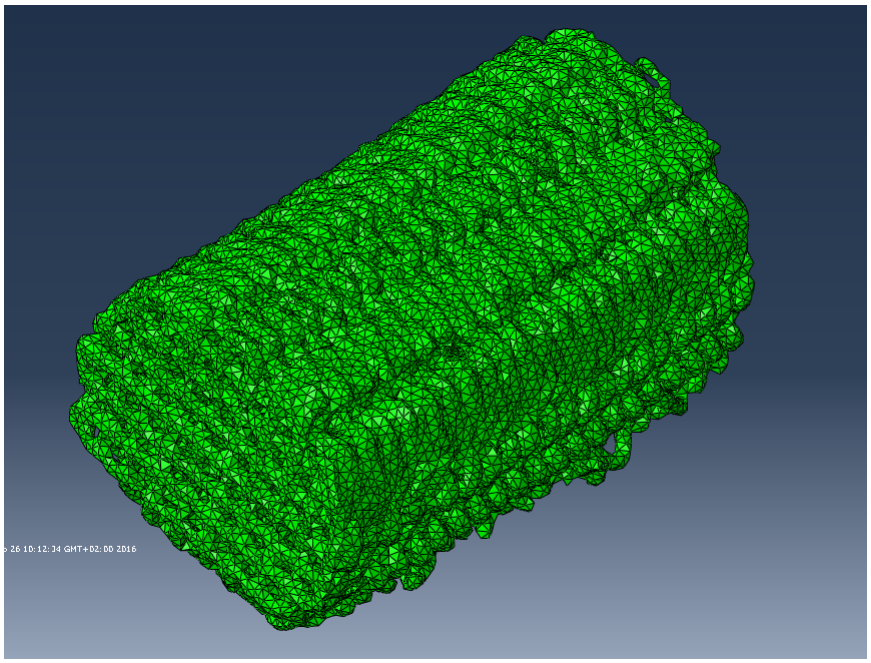

(b) μCT-based FE model

Figure 5.8: Comparison of STL-Based and μCT-Based Models - The image on the top shows the FE model that was created based on the STL-file of the Orthogonal Pattern, the bottom image illustrates the one based on the μCT images.

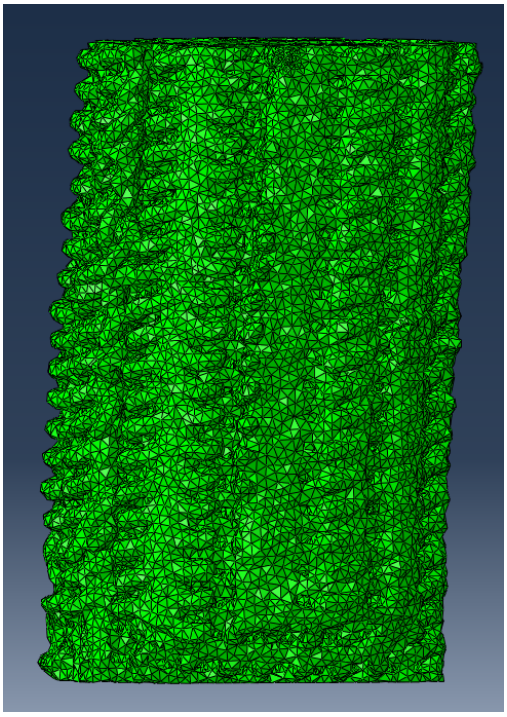

(a) The model does not stand completely upright, but is slightly skewed to the left.

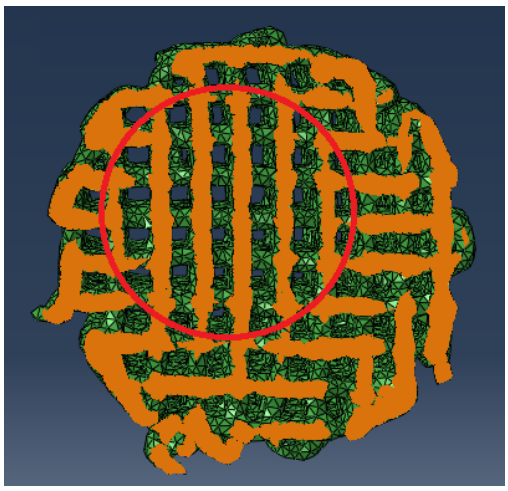

(b) This image shows a cross section view of the scaffold. It can be seen that the filament orientation within the red circle is opposed to the orientation outside of the circle.

Figure 5.9: Possible Defects in the μCT-Based Models - The image on the left shows how the scaffold is slightly skewed to the right. The right image illustrates an occurance of sagging.

Chapter 6

Conclusion

6.1 Summary

In Section 4, the simulation process was set up. Tetrahedrons were chosen to be used as elements for the finite element model and the Rankine criterion as the algorithm to find failed elements. With these settings, the simulation approximates the compression curves well.

The implemented simulation process was then used to compare different patterns in Section 5. The dataset that was used allowed for to mesh the patterns both from STL-files and from μCT images. The results of the STL-based simulations were consistent and delivered very good results. Even though the apparent properties were overestimated, the general shape and the ranking of the patterns were calculated correctly. The μCT-based simulations on the other hand differed quite significantly. Instead of a distinct peak after which basically the whole structure failed, they resulted in a platform, keeping up the total reaction force. Moreover, they failed to predict the ranking of the different patterns. Section 6.2 will explain in more detail about some potential problems and limitations that could be the reason of this behaviour.

6.2 Limitations

Several points are influencing the results and therefore have a limiting effect on the performance of the simulation algorithm.

Computational Power

The most obvious factor and comes into play with every simulation is the computational power. With more power, a denser mesh with more elements could be realised. This would not only improve the accuracy of the solution and guarantee convergence but also allow for a finite element model that resembles the original scaffold more closely and could therefore model more detailed structures. Additionally, it would also improve the runtime and therefore allow a better handling. Since the FE models used in this study

are already at the limit of the available computational power, no convergence analysis was conducted.

Different Specimen Used for Scanning and Mechanical Testing

As shown in Section 5.2 the variation in the apparent properties between the specimen even of the same pattern is quite considerable. The possible reasons for that are manifold and to determine which ones apply is out of the scope of this project. What can be said, however, is that this is a possible factor causing the overestimation of the properties by the simulation, since different specimen were used for μCT scanning and mechanical testing.

Differences in Material Properties

Another factor that could have influenced the results presented in Section 5 is the fact, that the bulk cylinders were produced from another bath of material than the rest of the patterned scaffolds. Even though the same procedure was followed to create the material, it can be assumed that certain differences do exist nevertheless. The actual magnitude of this difference is hard to estimate, tough.

Deviations Between Printed and Programmed Structures

The last point to consider are the structural deviations between the models based on the STL-files and the μCT images. It was shown in Section 5.4.2 that there are large differences between the programmed structure and the one that is actually achieved with by the 3D-printing. Additional to the obvious visible defects, there might be problems that are impossible to spot from the μCT images. There could be variations in the attachment strength of different filaments, differences in the microporosity that falls below the resolution threshold of the μCT scanner or occurance of microfractures. Most of these would indicate a weaker scaffold than predicted from the STL-based simulation.

6.3 Next Steps

To further improve the simulation process the following points could be addressed.

Further Validation

The validation of the simulation process during Project II (see Section 5) showed good results, especially for the STL-based simulations. To further confirm these results, more validation would be required. Especially the problem that different specimen are used for the mechanical testing and the μCT scanning would be ruled out if a similar dataset to the one used in Project I could be created. This means that additional specimen have to be μCT scanned while subjected to a compression test.

Convergence Analysis

Due to limiting factors in both computational power and available time, no convergence analysis was conducted. The slightly different results for the hexahedral and tetrahedral meshes indicate, that the solution has not converged fully yet, but is close to convergence. A convergence analysis should therefore be conducted.

References

[1] S. Bose, S. Vahabzadeh, and A. Bandyopadhyay, "Bone tissue engineering using 3d printing," *Materials Today*, vol. 16, no. 12, pp. 496–504, 2013, cited By 0. [Online]. Available: https://www.scopus.com/inward/record.uri?eid=2-s2.0-84890381496&partnerID=40&md5=8f3c66cfbf24af0d5e432c8e58fac7df

[2] H. Seitz, W. Rieder, S. Irsen, B. Leukers, and C. Tille, "Three-dimensional printing of porous ceramic scaffolds for bone tissue engineering," *Journal of Biomedical Materials Research - Part B Applied Biomaterials*, vol. 74, no. 2, pp. 782–788, 2005, cited By 285. [Online]. Available: https://www.scopus.com/inward/record.uri?eid=2-s2.0-23044436691&partnerID=40&md5=1370aaa5d5ff4c230bd5e335c45d041e

[3] M. Fernandez-Yague, S. Abbah, L. McNamara, D. Zeugolis, A. Pandit, and M. Biggs, "Biomimetic approaches in bone tissue engineering: Integrating biological and physicomechanical strategies," *Advanced Drug Delivery Reviews*, vol. 84, pp. 1–29, 2015, cited By 23. [Online]. Available: https://www.scopus.com/inward/record.uri?eid=2-s2.0-84929131367&partnerID=40&md5=8bc8037891f3a6fc00aedeef16bf6013

[4] D. Hutmacher, "Scaffolds in tissue engineering bone and cartilage," *Biomaterials*, vol. 21, no. 24, pp. 2529–2543, 2000, cited By 2533. [Online]. Available: https://www.scopus.com/inward/record.uri?eid=2-s2.0-0034672872&partnerID=40&md5=571b2a9a04832fa4cdecd67e62697fa5

[5] V. Karageorgiou and D. Kaplan, "Porosity of 3d biomaterial scaffolds and osteogenesis," *Biomaterials*, vol. 26, no. 27, pp. 5474–5491, 2005, cited By 2161. [Online]. Available: https://www.scopus.com/inward/record.uri?eid=2-s2.0-17844400927&partnerID=40&md5=3bdc9857a18824ff1bcaddc1aa8bee71

[6] J. An, J. E. M. Teoh, R. Suntornnond, and C. K. Chua, "Design and 3d printing of scaffolds and tissues," *Engineering*, vol. 1, no. 2, pp. 261 – 268, 2015, special Section: Advanced Materials and Materials GenomeMembersGuest Editors-in-Chief. [Online]. Available: http://www.sciencedirect.com/science/article/pii/S2095809916300716

[7] S. Peltola, F. Melchels, D. Grijpma, and M. Kellomäki, "A review of rapid prototyping techniques for tissue engineering purposes," *Annals of*

Medicine, vol. 40, no. 4, pp. 268–280, 2008, cited By 230. [Online]. Available: https://www.scopus.com/inward/record.uri?eid=2-s2.0-42449159656&partnerID=40&md5=0ea8708fa21c93ecb5c6510460e60c7a

[8] P. Miranda, A. Pajares, E. Saiz, A. Tomsia, and F. Guiberteau, "Mechanical properties of calcium phosphate scaffolds fabricated by robocasting," *Journal of Biomedical Materials Research - Part A*, vol. 85, no. 1, pp. 218–227, 2008, cited By 0. [Online]. Available: https://www.scopus.com/inward/record.uri?eid=2-s2.0-40449137701&partnerID=40&md5=1c969586f6704fc554643a29e9c09e9b

[9] J. Russias, E. Saiz, S. Deville, K. Gryn, G. Liu, R. Nalla, and A. Tomsia, "Fabrication and in vitro characterization of three-dimensional organic/inorganic scaffolds by robocasting," *Journal of Biomedical Materials Research - Part A*, vol. 83, no. 2, pp. 434–445, 2007, cited By 0. [Online]. Available: https://www.scopus.com/inward/record.uri?eid=2-s2.0-35048849578&partnerID=40&md5=3f24c833527dd0c63516ad73c7576431

[10] D. Pastorino, C. Canal, and M.-P. Ginebra, "Multiple characterization study on porosity and pore structure of calcium phosphate cements," *Acta Biomaterialia*, vol. 28, pp. 205–214, 2015, cited By 1. [Online]. Available: https://www.scopus.com/inward/record.uri?eid=2-s2.0-84947493444&partnerID=40&md5=71fddd5624c843abaf37748b342aa301

[11] D. Hutmacher, J. Schantz, C. Lam, K. Tan, and T. Lim, "State of the art and future directions of scaffold-based bone engineering from a biomaterials perspective," *Journal of Tissue Engineering and Regenerative Medicine*, vol. 1, no. 4, pp. 245–260, 2007, cited By 415. [Online]. Available: https://www.scopus.com/inward/record.uri?eid=2-s2.0-39149124477&partnerID=40&md5=b66cde757b529bcd08f38e34055b48b2

[12] R. LeGeros, "Calcium phosphate-based osteoinductive materials," *Chemical Reviews*, vol. 108, no. 11, pp. 4742–4753, 2008, cited By 435. [Online]. Available: https://www.scopus.com/inward/record.uri?eid=2-s2.0-57349168055&partnerID=40&md5=d12f142c2cce76b2f17fa29d4aa24500

[13] M. Espanol, R. Perez, E. Montufar, C. Marichal, A. Sacco, and M. Ginebra, "Intrinsic porosity of calcium phosphate cements and its significance for drug delivery and tissue engineering applications," *Acta Biomaterialia*, vol. 5, no. 7, pp. 2752–2762, 2009, cited By 78. [Online]. Available: https://www.scopus.com/inward/record.uri?eid=2-s2.0-69049094896&partnerID=40&md5=336a6301c73d52a72a45c3c3e6f8c06c

[14] R. Cancedda, P. Giannoni, and M. Mastrogiacomo, "A tissue engineering approach to bone repair in large animal models and in clinical practice," *Biomaterials*, vol. 28, no. 29, pp. 4240–4250, 2007, cited By 278. [Online].

Available: https://www.scopus.com/inward/record.uri?eid=2-s2.0-34547681854&partnerID=40&md5=aed066dd9dafabe4849498e0947dbf5c

[15] J. Jones, G. Poologasundarampillai, R. Atwood, D. Bernard, and P. Lee, "Non-destructive quantitative 3d analysis for the optimisation of tissue scaffolds," *Biomaterials*, vol. 28, no. 7, pp. 1404–1413, 2007, cited By 121. [Online]. Available: https://www.scopus.com/inward/record.uri?eid=2-s2.0-33845607627&partnerID=40&md5=924f879e8c3f386f2bec09b5a0c7f610

[16] O. Zienkiewicz, R. Taylor, and J. Zhu, *The Finite Element Method: its Basis and Fundamentals: Seventh Edition*, 2013, cited By 0. [Online]. Available: https://www.scopus.com/inward/record.uri?eid=2-s2.0-84903927842&partnerID=40&md5=2ec8698bf1d5ad09a5ea885e3d7bce23

[17] C. Sandino, J. Planell, and D. Lacroix, "A finite element study of mechanical stimuli in scaffolds for bone tissue engineering," *Journal of Biomechanics*, vol. 41, no. 5, pp. 1005–1014, 2008, cited By 96. [Online]. Available: https://www.scopus.com/inward/record.uri?eid=2-s2.0-40249089772&partnerID=40&md5=5cca55134f7892ebf4eb9f0e7d20ce01

[18] S. Gómez, M. Vlad, J. López, and E. Fernández, "Design and properties of 3d scaffolds for bone tissue engineering," *Acta Biomaterialia*, vol. 42, pp. 341–350, 2016, cited By 0. [Online]. Available: https://www.scopus.com/inward/record.uri?eid=2-s2.0-84983356812&partnerID=40&md5=01d6d54f9f2747c4d4e48d35cc6223a9

[19] S. Jaecques, H. Van Oosterwyck, L. Muraru, T. Van Cleynenbreugel, E. De Smet, M. Wevers, I. Naert, and J. Vander Sloten, "Individualised, micro ct-based finite element modelling as a tool for biomechanical analysis related to tissue engineering of bone," *Biomaterials*, vol. 25, no. 9, pp. 1683–1696, 2004, cited By 113. [Online]. Available: https://www.scopus.com/inward/record.uri?eid=2-s2.0-0345862402&partnerID=40&md5=084842e925a19da9ce30ed4cebc74a75

[20] R. Hambli, "Micro-ct finite element model and experimental validation of trabecular bone damage and fracture," *Bone*, vol. 56, no. 2, pp. 363–374, 2013, cited By 19. [Online]. Available: https://www.scopus.com/inward/record.uri?eid=2-s2.0-84880943524&partnerID=40&md5=6213745df46df543da03b6cab842a1b4

[21] P. Miranda, A. Pajares, and F. Guiberteau, "Finite element modeling as a tool for predicting the fracture behavior of robocast scaffolds," *Acta Biomaterialia*, vol. 4, no. 6, pp. 1715–1724, 2008, cited By 30. [Online]. Available: https://www.scopus.com/inward/record.uri?eid=2-s2.0-53649102538&partnerID=40&md5=cb28de4787c3d16e04a7d8abe9db9780

[22] Q. Fang and D. A. Boas, "Tetrahedral mesh generation from volumetric binary and gray-scale images," in *Proceedings of the Sixth IEEE International Conference on Symposium on Biomedical Imaging: From Nano to Macro*, ser. ISBI'09.

Piscataway, NJ, USA: IEEE Press, 2009, pp. 1142–1145. [Online]. Available: http://dl.acm.org/citation.cfm?id=1699872.1700164

[23] R. Hambli and S. Allaoui, "A robust 3d finite element simulation of human proximal femur progressive fracture under stance load with experimental validation," *Annals of Biomedical Engineering*, vol. 41, no. 12, pp. 2515–2527, 2013, cited By 9. [Online]. Available: https://www.scopus.com/inward/record.uri?eid=2-s2.0-84896712375&partnerID=40&md5=8fddf6c8891aeadc108369a9885202c2

[24] "CGAL, Computational Geometry Algorithms Library," http://www.cgal.org.

[25] H. Si, "Tetgen, a delaunay-based quality tetrahedral mesh generator," *ACM Trans. Math. Softw.*, vol. 41, no. 2, pp. 11:1–11:36, Feb. 2015. [Online]. Available: http://doi.acm.org/10.1145/2629697

[26] C. Schneider, W. Rasband, and K. Eliceiri, "Nih image to imagej: 25 years of image analysis," *Nature Methods*, vol. 9, no. 7, pp. 671–675, 2012, cited By 5979. [Online]. Available: https://www.scopus.com/inward/record.uri?eid=2-s2.0-84863205849&partnerID=40&md5=b4f937ef9f465a37958eaebe2fcb4dcc

[27] Y. Maazouz, E. B. Montufar, J. Guillem-Marti, I. Fleps, C. Ohman, C. Persson, and M. P. Ginebra, "Robocasting of biomimetic hydroxyapatite scaffolds using self-setting inks," *J. Mater. Chem. B*, vol. 2, pp. 5378–5386, 2014. [Online]. Available: http://dx.doi.org/10.1039/C4TB00438H

[28] S. Tadepalli, A. Erdemir, and P. Cavanagh, "Comparison of hexahedral and tetrahedral elements in finite element analysis of the foot and footwear," *Journal of Biomechanics*, vol. 44, no. 12, pp. 2337–2343, 2011, cited By 21. [Online]. Available: https://www.scopus.com/inward/record.uri?eid=2-s2.0-79960717454&partnerID=40&md5=dc9c7e67e6edc519b2757b0b5e8a5253

[29] A. Ramos and J. Simões, "Tetrahedral versus hexahedral finite elements in numerical modelling of the proximal femur," *Medical Engineering and Physics*, vol. 28, no. 9, pp. 916–924, 2006, cited By 68. [Online]. Available: https://www.scopus.com/inward/record.uri?eid=2-s2.0-33747751643&partnerID=40&md5=a77b6a37a554095ea1b0a3f26a853b50

[30] D. Payen and K.-J. Bathe, "Improved stresses for the 4-node tetrahedral element," *Computers and Structures*, vol. 89, no. 13-14, pp. 1265–1273, 2011, cited By 14. [Online]. Available: https://www.scopus.com/inward/record.uri?eid=2-s2.0-79956145286&partnerID=40&md5=1e58e293abe521f951e80b777088790e

[31] B. González, "Final project: Caracterización mecánica de estructuras macroporosas fabricadas por extrusión aditiva de pasta cerámica."